Optimal DC Voltage and Current Control of an LCC HVDC System to Improve Real-Time Frequency Regulation in Rectifier- and Inverter-Side Grids

Do-Hoon Kwon, *Member*, *IEEE* and Young-Jin Kim, *Member*, *IEEE*, and Oriol Gomis-Bellmunt, *Senior Member*, *IEEE*

***Abstract*—High-voltage direct-current (HVDC) systems for constant or intermittent power delivery have recently been developed further to support grid frequency regulation (GFR). This paper proposes a new control strategy for a line-commutated converter-based (LCC) HVDC system, wherein the dc-link voltage and current are optimally regulated to improve real-time GFR in both rectifier- and inverter-side grids. A dynamic model of an LCC HVDC system is developed using the dc voltage and current as input variables, and is integrated with feedback loops for inertia emulation and droop control. A linear quadratic Gaussian (LQG) controller is also designed for optimal secondary frequency control, while mitigating conflict between the droop controllers of HVDC converters. An eigenvalue analysis is then conducted, focusing on the effects of model parameters and controller gains on the proposed strategy. Simulation case studies are performed using the models of a real HVDC system and a CIGRE benchmark system. The case study results confirm that the proposed strategy enables the HVDC system to improve GFR, in coordination with generators in both-side grids, by exploiting the fast dynamics of HVDC converters. The proposed strategy is also effective under various conditions for the LQG parameters, inertia emulation, and droop control.**

***Index Terms*— dc voltage and current, droop control, frequency regulation, high-voltage direct-current system, line-commutated converter, linear quadratic Gaussian, inertia emulation.**

NOMENCLATURE

A. Acronyms

GFR	grid frequency regulation
HVDC	high-voltage direct-current
IPM	inverse power modeling
LCC	line-commutated converter-based
LQG	linear quadratic Gaussian
PFC	primary frequency control
SFC	secondary frequency control
RES	renewable energy source
VSC	voltage-source converter-based
WF	wind farm

B. Sets and Indices

a, b, c	coefficients for small-signal modeling of HVDC system
m, n	coefficients for estimation of $\Delta I_{dci}/\Delta I_{dci\_ref}$ and $\Delta V_{dcr}/\Delta V_{dcr\_ref}$
r, i	subscripts for variables and parameters related to the HVDC rectifier and inverter
$ref, 0$	subscripts for reference and nominal values
(x, β, H)	set of subscripts and variables [i.e., (r, α, V) or (i, γ, I)]
$\mathbf{E}$	subscript for an augmented small-signal model

C. HVDC System

V_{cr}, I_{ci}	dc voltage and current controlled via inertia emulation
V_{dc}	dc-link voltage
V_{dcr}, V_{dci}	dc voltages of the rectifier and inverter
I_c	charging current of the dc-link capacitor
I_{dcr}, I_{dci}	dc currents of the rectifier and inverter
P_{dcr}, P_{dci}	dc power transfer of the rectifier and inverter
R, L, C	dc-link resistance, inductance, and capacitance
N	number of bridges connected within series in HVDC converters
TR_r, TR_i	converter transformer tap ratios
V_{drop}	dc voltage drop between the rectifier and inverter
V_{lr}, V_{li}	secondary voltages of the converter transformers
X_{cr}, X_{ci}	reactance of the converter transformers
α, γ	firing and extinction angles
μ_r, μ_i	overlap angles of the switching valves
T_{fr}, T_{fi}	time constants of the low pass filters
T_k, $T_{dcf1,2}$	time constants of the dc link and dc harmonic filters
T_r, T_i	equivalent time constants of the rectifier and inverter
K_r, K_i	gains for dc voltage-power droop control
R_r, R_i	gains for frequency-power droop control
V_r, V_i	inertia emulation gains
k_{pr}, k_{ir}	PI controller gains for V_{dcr} control
k_{pi}, k_{ii}	PI controller gains for I_{dci} control
$KP_{r,i}$, $KI_{r,i}$	PI controller gains for the SFCs of the rectifier and inverter

D. Rectifier- and Inverter-Side Grids

f_r, f_i	frequencies of both-side grids
D_r, D_i	load damping coefficients of both-side grids
M_r, M_i	moments of inertia of both-side grids
P_{gr}, P_{gi}	power outputs of conventional generators
P_{gr_ref}, P_{gi_ref}	reference power outputs of conventional generators
P_{lr}, P_{li}	load demand in both-side grids
P_{tr}, P_{ti}	reference power outputs delivered from governors to steam turbines
P_w	wind power generation
T_{gr}, T_{gi}	time constants of governors
T_{tr}, T_{ti}	time constants of steam turbines
R_{gr}, R_{gi}	gains for frequency-power droop control

E. Coordinated Control of the HVDC System and Generators

$\mathbf{A}$, $\mathbf{B_r}$, $\mathbf{B_w}$, $\mathbf{C}$	coefficient matrices of the small-signal model of the HVDC system and generators
$\mathbf{A_E}$, $\mathbf{B_{rE}}$, $\mathbf{B_{wE}}$, $\mathbf{C_E}$	coefficient matrices of the augmented small-signal model of the HVDC system and generators
$\mathbf{A_s}$	sub-matrix in $\mathbf{A_E}$
$\mathbf{X}$, $\mathbf{Y}$	states and outputs of the small-signal model of the HVDC system and generators
$\mathbf{X_E}$, $\mathbf{Y_E}$	states and outputs of the augmented model
$\widehat{\mathbf{X_E}}$	estimate of $\mathbf{X_E}$ derived using the Kalman filter
$\mathbf{d}$, $\mathbf{n}$	input and output disturbances
$\mathbf{r}$, $\mathbf{w}$	controllable and uncontrollable inputs of the small-signal model of the HVDC system and generators

Manuscript received Oct. 12, 2019 (corresponding author: Y. Kim).

D. H. Kwon is with Korea Electrotechnology Research Institute (KERI), Uiwang-si, Gyeonggi-do, 16029, Korea (e-mail: dhkwon@keri.re.kr).

Y. Kim is with the Department of Electrical Engineering, Pohang University of Science and Technology, Pohang, Gyungbuk 37673, Korea (e-mail: powersys@postech.ac.kr).

O. Gomis-Bellmunt is with the Centre d'Innovacio Tecnologica en Convertidors Estatics i Accionaments, Departament d'Enginyeria Electrica, Universitat Politecnica de Catalunya, Barcelona 08028, Spain (oriol.gomis@upc.edu)

K	LQG gain matrix minimizing the cost function J
Q, **R**	diagonal matrices with weighting coefficients for state and input variables
V	transfer function matrix between **w** and $\mathbf{Y_E}$
J	cost function of LQG regulation
L_p, L_c	equipment lifetime estimated using the proposed and conventional strategies
n, n_V, n_f	endurance coefficients of factors affecting lifetime

I. Introduction

ADVANCES in power conversion and control technologies have brought about a renewed interest in the applications of high-voltage direct-current (HVDC) systems for reliable and economical inter-regional delivery of electric power. In particular, several ongoing projects worldwide [1]–[3] aim to facilitate the connection of large-scale renewable energy sources (RESs) in remote host regions with distant load centers via line-commutated converter-based (LCC) HVDC systems ranging from 500 MW to 1,500 MW in size. For example, an LCC HVDC system installed in the Midwest region of the United States has been reported to deliver approximately 25% of the power generated by the wind turbines, with a total capacity of 16 GW, to the Eastern Interconnection [4]. Control strategies for mature, trusted LCC HVDC technology have been continuously improved, alleviating the impact of intermittent wind power on grid frequency regulation (GFR) by exploiting the fast responses of HVDC converters.

As listed in Table I, the real-time GFR of LCC HVDC systems has been the topic of many papers. For example, in [5], an HVDC rectifier station was connected to a wind farm (WF). The rectifier firing angle or, equivalently, dc-link current was controlled for GFR in the rectifier-side grid. In [6], an HVDC system was used as an interface between a WF and an inverter-side network, so that its rotational kinetic energy could be exploited in the form of electrical inertia to improve GFR. The paper [7] analyzed the effects of a short circuit ratio and a dc inertia constant on GFR in a weak grid, which was linked to both WF and LCC HVDC systems. In [8], a fuzzy inference system was integrated into the damping controller of an HVDC inverter to suppress oscillations of the inverter-side frequency and ac voltage, resulting from a short-circuit fault at the point of common coupling. However, in [5]–[8], an LCC HVDC system was controlled to support GFR only in either the inverter- or rectifier-side network, because the other-side network included only WFs, rather than synchronous generators and loads.

Recently, GFR has been considered on both sides of the LCC HVDC system. For example, in [9], the hourly optimal power flow was calculated by reference to the fast-acting corrective control of an LCC HVDC system when the HVDC bi-pole block resulted in large frequency deviations in the sending- and receiving-end grids. In [10], a four-state nonlinear model was presented to determine the interaction between the rectifier- and inverter-side grids and develop HVDC firing angle controllers and a WF droop controller. Considering inter-grid coupling, optimal control schemes can be adopted to better utilize HVDC systems. For example, in [11] and [12], linear quadratic regulators (LQRs) were used to reduce variation in the voltage and rotor angle, respectively, and hence enhance the damping of inter-area power oscillations; however, the HVDC system models were relatively simple and droop controllers were not considered.

In [9]–[11], the dc-link voltage of the HVDC system was simply maintained at the rated value. In practice, LCC HVDC converters can operate under normal conditions, with short-term under- and over-voltages of the dc link, as reported in field test results [13], [14]. Recently, a few studies have explored time-varying control of the dc-link voltage, mainly for voltage-source converter-based (VSC) HVDC systems. For example, in [15], a VSC HVDC system was controlled with the operating range of the dc-link voltage varying from approximately 0.98 pu to 1.04 pu for a 5% variation in load demand. In [16], the energy stored in the dc link was combined with the frequency support capabilities of wind turbines. Time-varying control of the dc-link voltage can also be applied to LCC HVDC systems. For example, in [17] and [18], dc-link voltage control improved the capabilities of LCC HVDC systems principally in the contexts of short-term power transfer and reactive power control, respectively.

This paper proposes a new control strategy for an LCC HVDC system, in which the optimal control of dc-link voltage and current is achieved in real time to improve GFR in both the rectifier- and inverter-side networks. A small-signal model of the HVDC system is developed using the dc voltage and current references as input variables, and validated via comparison with the comprehensive models of a real HVDC system and a CIGRE benchmark system. The HVDC converters support real-time GFR via primary (PFC) and secondary frequency control (SFC). For PFC, the converters are integrated with feedback loops for frequency- and dc voltage-power droop control, and also allow inertial response emulation. A linear quadratic Gaussian (LQG) controller, combining an LQR with

TABLE I. SPECIFICATIONS, MODELS, AND GRID-LEVEL CONTROLLERS OF LCC HVDC SYSTEMS

Ref.	(a) Specifications				(b) Modelling						(c) Grid-level controllers				
	P_{dc0} [MW]	V_{dc0} [kV]	V_{dc}	varying power	input references		output	converters	dc link	filters	objective	target grids	inertial response	droop	SFC
Proposed	150	184	varying	P	V_{dcr}	I_{dci}	V_{dc}, $P_{dci,r}$	avg.	T	ac, dc	opt. GFR	both	O	O	LQG
[5]	1000	500	constant	P	I_{dcr}		I_{dcr}	switch	RL circuit	ac	GFR	rec.		O	PI
[6]	500	500			P_{dcr}	γ	P_{dcr}	avg.			GFR	inv.	O	O	
[7]	1000	500			f_r	γ		avg.	T	ac	GFR	rec.	O		
[8]	100	200			P_{dcr}	I_{dci}	V_{dcr}, I_{dci}	avg.	T	dc	GFR	inv.		O	PID
[10]	1000	500			f_r	γ	P_{dci}	avg.	T		GFR	both		O	
[11]	50	100			I_{dcr}	V_{dci}	P_{acr}, Q_{aci}	injection	T		opt. damping	both			LQG
[12]	–	–	varying		I_{dcr}	V_{dci}	$P_{aci,r}$, Q_{aci}	injection	T		opt. damping	both			LQG
[16]	300	300			P_{dcr}	V_{dci}	P_{dcr}	switch	Π		GFR	inv.	O	O	PI
[17]	150	184			V_{dcr}	I_{dci}	P_{dci}	avg.	T		GFR	inv.		O	PI
[18]	250	500		P, Q	P_{dcr}	Q_{aci}	P_{dcr}, Q_{aci}	switch	T	ac	voltage reg.	inv.			

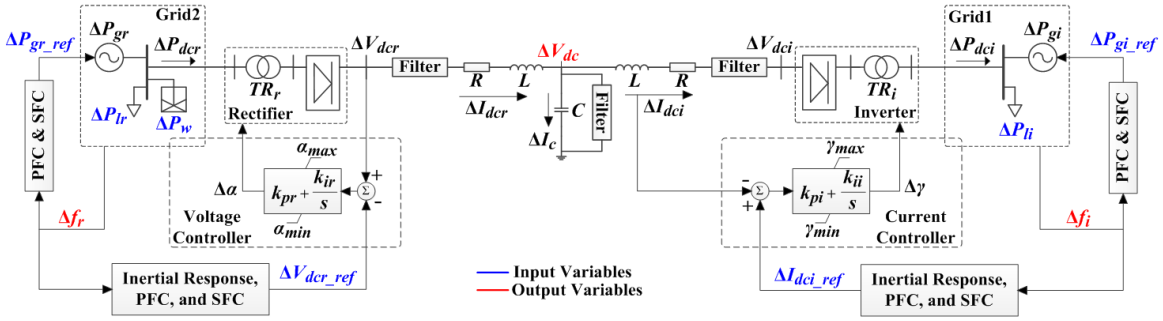

Fig. 1. A schematic diagram of the proposed control strategy for an LCC HVDC system to support real-time GFR in the rectifier- and inverter-side ac networks.

a Kalman filter, is also incorporated into the feedback loops to achieve optimal SFC, minimizing the weighted sum of instantaneous and accumulated deviations of the dc-link voltage and grid frequencies in the rectifier- and inverter-side grids. An eigenvalue analysis is then conducted to evaluate the performance of the proposed control strategy with variation in the model parameters and controller gains of the HVDC system. Simulation case studies are also carried out to demonstrate that the proposed strategy effectively improves real-time GFR in the context of variation in load demand and WF power generation under various conditions on the LQG weighting factors and the inertia emulation and droop control approaches.

The main contributions of this paper are summarized below:

- To the best of our knowledge, this is the first study reporting optimal dc voltage and current control of an LCC HVDC system for real-time GFR of both rectifier- and inverter-side grids using an LQG controller.
- The methods for inertial response emulation and frequency- and dc voltage-power droop control are integrated to exploit the fast responses of HVDC converters. The LQG controller resolves conflicts between the droop controllers.
- A small-signal model is implemented whereby the dc voltage and current can be separately controlled at distinct HVDC terminals. The small-signal model is simple, but successfully reflects dynamic variations in dc voltage, current, and power.
- The effectiveness of the proposed optimal control strategy is verified using the models of a real HVDC system and a CIGRE benchmark system as the load demand, LQG parameters, and PFC type vary.

II. Dynamic Model of LCC HVDC System for GFR via the Control of DC-link Voltage and Current

Fig. 1 shows a schematic diagram of the proposed strategy, in which an LCC HVDC system supports real-time GFR in the rectifier- and inverter-side grids. The rectifier and inverter use the same architecture and inner feedback loops to control ΔV_{dcr} and ΔI_{dci}, respectively. The dc link is characterized using a T-model, where ΔP_{dcr} flows into the rectifier and ΔP_{dci} flows from the inverter. Under normal grid conditions, the off-nominal frequencies Δf_i and Δf_r reflect the load demand variations ΔP_{li} and ΔP_{lr} in the both-side grids and the intermittent power outputs ΔP_w of the WF in the rectifier-side grid. The proposed strategy focuses on mitigating Δf_i and Δf_r via optimal control of ΔV_{dcr} and ΔI_{dci} before frequency deviations become severe enough to adversely affect ac network operations. Analysis of the proposed strategy under abnormal conditions (e.g., ac line faults and commutation failures) will be conducted in future work.

A. Dynamic Model of LCC HVDC System

The dc-link voltage, current, and power at the terminals of the rectifier and inverter can be represented [19] as:

$$V_{dcx} = \frac{3\sqrt{2}N}{\pi TR_x} V_{lx} \cos\beta - \frac{3X_{cx}N}{\pi} I_{dcx} \ , \tag{1}$$

$$I_{dcx} = \frac{V_{lx}}{\sqrt{2}X_{cx}TR_x}\left(\cos\beta - \cos\left(\beta+\mu_x\right)\right) \ , \tag{2}$$

$$P_{dcx} = V_{dcx} I_{dcx} \ , \tag{3}$$

$$= \frac{3N}{4\pi X_{cx}}\left(\frac{V_{lx}}{TR_x}\right)^2 \left\{\cos\left(2\beta\right) - \cos 2\left(\beta+\mu_x\right)\right\} \ . \tag{4}$$

where descriptions of the variables are provided in Section IV (see Table II). Note that the subscript x is replaced with r and i to indicate the variables related to the rectifier and inverter, respectively. Moreover, β corresponds to the firing and extinction angles (i.e., α and γ, respectively). As shown in Fig. 1, $\Delta\alpha$ and $\Delta\gamma$ can be estimated as:

$$\Delta\beta = \pm H_{dcx0}^{-1}\left(k_{px} + k_{ix}/s\right)\left(\Delta H_{dcx} - \Delta H_{dcx\_ref}\right) \ , \tag{5}$$

where H corresponds to V and I for the voltage and current controllers, respectively: i.e., $(x, \beta, H) = (r, \alpha, V)$ or (i, γ, I).

For the inverter, the linearized forms of (1), (2), and (4) correspond to (6)–(8), respectively:

$$\Delta V_{dci} = -a_{1i}\sin\gamma_0 \Delta\gamma - a_{2i}\Delta I_{dci} = -b_{1i}\Delta\gamma - a_{2i}\Delta I_{dci} \ , \tag{6}$$

$$\Delta I_{dci} = \frac{1}{a_{3i}}\left\{\sin\left(\gamma_0+\mu_{i0}\right) - \sin\gamma_0\right\}\Delta\gamma + \frac{1}{a_{3i}}\sin\left(\gamma_0+\mu_{i0}\right)\Delta\mu_i \ , \tag{7}$$

$$= \left(b_{2i}\Delta\gamma + b_{3i}\Delta\mu_i\right)/a_{3i} \ ,$$

$$\Delta P_{dci} = -2a_{4i}\sin\left(2\gamma_0\right)\Delta\gamma + 2a_{4i}\sin 2\left(\gamma_0+\mu_{i0}\right)\left(\Delta\gamma+\Delta\mu_i\right) \ , \tag{8}$$

$$= b_{4i}\Delta\gamma + b_{5i}\Delta\mu_i \ ,$$

where coefficients a and b are provided in the Appendix. By substituting (7) into (8), ΔP_{dci} can also be expressed as:

$$b_{3i}\Delta P_{dci} = a_{3i}b_{5i}\Delta I_{dci} + \left(b_{3i}b_{4i} - b_{2i}b_{5i}\right)\Delta\gamma \ . \tag{9}$$

Moreover, using (3) and (6), ΔP_{dci} is given in another form as:

$$\Delta P_{dci} \approx I_{dci0}\Delta V_{dci} + V_{dci0}\Delta I_{dci} = \left(V_{dci0} - a_{2i}I_{dci0}\right)\Delta I_{dci} - b_{1i}I_{dci0}\Delta\gamma \ . \tag{10}$$

Then, by integrating (9) and (10) into (5), the transient response $\Delta I_{dci}/\Delta I_{dci\_ref}$ of the inverter can be represented as:

$$\left(a_{3i}b_{5i}-b_{3i}c_{1i}\right)\Delta I_{dci}=a_{5i}c_{2i}\left(k_{pi}+\frac{k_{ii}}{s}\right)\left(\Delta I_{dci\_ref}-\Delta I_{dci}\right), \quad (11)$$

which can be equivalently expressed as (12) (see below; the coefficients c are also shown in the Appendix). For both real and benchmark HVDC systems, $\Delta I_{dci}/\Delta I_{dci\_ref}$ in (12) can be approximated to a strictly proper first-order transfer function, because the ratio of m_3 to m_1 has a magnitude comparable to that of V_{dcr0} to I_{dcr0}: e.g., V_{dcr0} = 184,000 V, I_{dcr0} = 407.6 A, and $m_3/m_1 = 7.7\times10^{-3}$ for a real 150-MW HVDC system [20].

Similarly, for the rectifier, the linearized forms of (1), (2), and (4) correspond to (13)–(15), respectively:

$$\Delta V_{dcr}=-a_{1r}\sin\alpha_0\Delta\alpha-a_{2r}\Delta I_{dcr}=-b_{1r}\Delta\alpha-a_{2r}\Delta I_{dcr}\ , \quad (13)$$

$$\Delta I_{dcr}=\frac{1}{a_{3r}}\left\{\sin\left(\alpha_0+\mu_{r0}\right)-\sin\alpha_0\right\}\Delta\alpha+\frac{1}{a_{3r}}\sin\left(\alpha_0+\mu_{r0}\right)\Delta\mu_r\ , \quad (14)$$
$$=\left(b_{2r}\Delta\alpha+b_{3r}\Delta\mu_r\right)/a_{3r}\ ,$$

$$\Delta P_{dcr}=-2a_{4r}\sin\left(2\alpha_0\right)\Delta\alpha+2a_{4r}\sin2\left(\alpha_0+\mu_{r0}\right)\left(\Delta\alpha+\Delta\mu_r\right)\ , \quad (15)$$
$$=b_{4r}\Delta\alpha+b_{5r}\Delta\mu_r\ .$$

By combining (13)–(15), ΔP_{dcr} is expressed as:

$$a_{2r}b_{3r}\Delta P_{dcr}=-a_{3r}b_{5r}\Delta V_{dcr}+\left(a_{2r}b_{3r}b_{4r}-a_{2r}b_{2r}b_{5r}-a_{3r}b_{1r}b_{5r}\right)\Delta\alpha\ . \quad (16)$$

Moreover, from (3) and (13), ΔP_{dcr} is given in another form as:

$$a_{2r}\Delta P_{dcr}\approx a_{2r}\left(I_{dcr0}\Delta V_{dcr}+V_{dcr0}\Delta I_{dcr}\right)\ , \quad (17)$$
$$=\left(a_{2r}I_{dcr0}-V_{dcr0}\right)\Delta V_{dcr}-b_{1r}V_{dcr0}\Delta\alpha\ .$$

Integration of (5), (16) and (17) gives the transient response $\Delta V_{dcr}/\Delta V_{dcr\_ref}$ of the rectifier:

$$\frac{\Delta V_{dcr}}{\Delta V_{dcr\_ref}}=\frac{a_{5r}c_{1r}k_{pr}s+a_{5r}c_{1r}k_{ir}}{\left(a_{5r}c_{1r}k_{pr}-c_{2r}\right)s+a_{5r}c_{1r}k_{ir}}=\frac{n_3s+n_2}{n_1s+n_2}\ , \quad (18)$$

which can be further approximated to:

$$\frac{\Delta V_{dcr}}{\Delta V_{dcr\_ref}}\approx\frac{1}{\left(n_1/n_2\right)s+1}\ . \quad (19)$$

This is because the ratio of n_3 to n_1 is determined mainly by $1/V_{dcr0}$; for example, n_3/n_1 is less than 0.01 for the real and benchmark HVDC systems [20], [21]. As shown in (12) and (19), the responsibilities to regulate ΔI_{dci} and ΔV_{dcr} can be kept distinct and assigned to separate HVDC terminals.

In addition, given the symmetry of the dc-link model, the relationship between ΔV_{dci} and ΔV_{dcr} can be represented as:

$$\Delta V_{dci}=\Delta V_{dcr}-\left(R+sL\right)\Delta I_{dcr}-\left(R+sL\right)\Delta I_{dci}\ , \quad (20)$$

and $$\Delta I_{dcr}=\Delta I_{dci}+sC\Delta V_{dc}\ , \quad (21)$$

where $\Delta V_{dc} = 0.5\cdot(\Delta V_{dcr}+\Delta V_{dci})$ is the voltage variation at the mid-point of the dc link. By substituting (21) into (20), ΔV_{dci} can be equivalently represented as:

$$\Delta V_{dci}=\frac{1-0.5sC\left(R+sL\right)}{1+0.5sC\left(R+sL\right)}\Delta V_{dcr}-\frac{2\left(R+sL\right)}{1+0.5sC\left(R+sL\right)}\Delta I_{dci}\ . \quad (22)$$

In practice, it is common that L and C (and, consequently, $L\cdot C$ and $R\cdot C$) are very small [22]–[24]. Under the common conditions of real HVDC systems, (22) can be simplified to:

$$\Delta V_{dci}=\frac{1/s^2-0.5RC/s-0.5LC}{1/s^2+0.5RC/s+0.5LC}\Delta V_{dcr}-\frac{2\left(R/s^2+L/s\right)}{1/s^2+0.5RC/s+0.5LC}\Delta I_{dci},$$
$$\approx\frac{1/s^2-0.5RC/s}{1/s^2+0.5RC/s}\Delta V_{dcr}-\frac{2\left(R/s^2+L/s\right)}{1/s^2+0.5RC/s}\Delta I_{dci}\ ,$$
$$\approx\frac{1/s^2}{1/s^2}\Delta V_{dcr}-\frac{2R/s^2}{1/s^2+0.5RC/s}\Delta I_{dci}\ ,$$
$$=\Delta V_{dcr}-\frac{2R}{sT_k+1}\Delta I_{dci}\ ,\qquad \text{where } T_k=RC/2\ . \quad (23)$$

In (23), the second term represents dynamic variation in the voltage drop along the dc link. Note that (23) still reflects the dc-link operation in the steady state (i.e., $V_{dci} = V_{dcr} - 2R\cdot I_{dci}$). Using (23), ΔP_{dci} can be represented as:

$$\Delta P_{dci}\approx I_{dci0}\Delta V_{dci}+V_{dci0}\Delta I_{dci}\approx I_{dci0}\left(\Delta V_{dcr}-\frac{2R}{sT_k+1}\Delta I_{dci}\right)+V_{dci0}\Delta I_{dci}\ . \quad (24)$$

Furthermore, in practice, the variation in the capacitor charging current ΔI_c (i.e., $sC\Delta V_{dc}$ in (21)) is negligible compared to ΔI_{dcr} and ΔI_{dci} given the small values of C and ΔV_{dc}. Therefore, (21) can be approximated to $\Delta I_{dcr} \approx \Delta I_{dci}$, enabling ΔP_{dcr} to be expressed as:

$$\Delta P_{dcr}\approx I_{dcr0}\Delta V_{dcr}+V_{dcr0}\Delta I_{dcr}\approx I_{dcr0}\Delta V_{dcr}+V_{dcr0}\Delta I_{dci}\ . \quad (25)$$

It can be seen in (24) and (25) that ΔP_{dci} and ΔP_{dcr} differ only slightly under normal operating conditions (i.e., $V_{dcr0} = V_{dci0}$ = 1 pu and $I_{dcr0} = I_{dci0}$ = 1 pu). Using the analysis above, the original and simplified small-signal models of the LCC HVDC system can be implemented as shown in Fig. 2(a) and (b), respectively. Note that the variation in ac voltage and reactive power at HVDC terminals is not considered due to marginal effects on the GFR. The profiles of ΔV_{dcr}, ΔI_{dci}, and $\Delta P_{dcr(i)}$ obtained from (5)–(25) remain highly consistent with those acquired from the

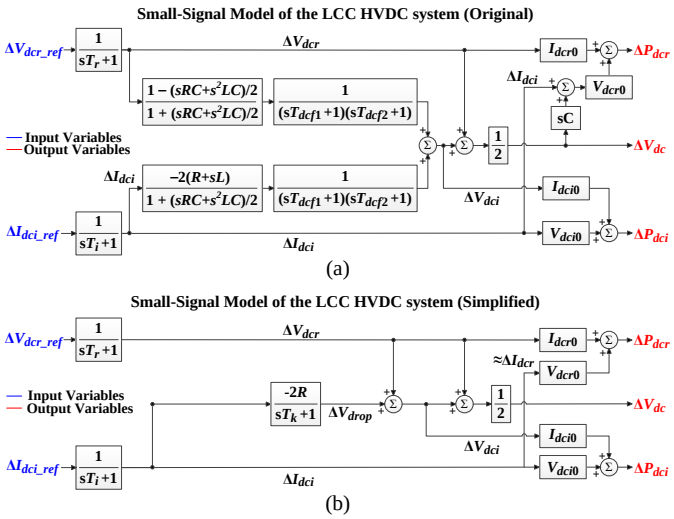

Fig. 2. (a) Original and (b) simplified small-signal models of the HVDC system considering the dynamics of the dc link, converters, and inner feedback loops.

$$\frac{\Delta I_{dci}}{\Delta I_{dci\_ref}}=\frac{k_{pi}a_{5i}c_{2i}\cdot s+k_{ii}a_{5i}c_{2i}}{\left\{a_{3i}b_{5i}-b_{3i}c_{1i}+k_{pi}a_{5i}c_{2i}\right\}\cdot s+k_{ii}a_{5i}c_{2i}}=\frac{m_3s+m_4}{m_1s+m_2}=\frac{m_3}{m_1}+\frac{m_4-\left(m_2m_3/m_1\right)}{m_1s+m_2}\approx\frac{1}{\left(m_1/m_2\right)s+1} \quad (12)$$

comprehensive MATLAB/ SIMULINK model (see Section IV-B).

In general, dc filters are installed at HVDC terminals to mitigate dc-side harmonic currents and voltages [25]. In the original small-signal model, the operations of dc filters were represented using second-order transfer functions [26], as shown in Fig. 2(a). For brevity, the simplified model is implemented without the dc filters because, in (23), the relationships of ΔV_{dci} with ΔV_{dcr} and ΔI_{dci} have already been represented using the zero- and first-order characteristic equations (i.e., $\Delta_V(s) = 1$ and $\Delta_I(s) = sT_k+1$, respectively). This does not compromise the consistency of the original and simplified small-signal models, as discussed in Section IV-B. In other words, the proposed strategy is not conditional on the nature of the dc harmonic filters.

B. Real-time GFR Support Provided by LCC HVDC System

Fig. 3 shows a block diagram of the proposed control strategy, where the LCC HVDC system supports the GFR on the rectifier- and inverter-side grids. It includes the dynamic model of the HVDC system developed in Section II-A. The GFR support afforded by the proposed strategy is effective under the common operating conditions of the sending-end grid, where the total power generation (i.e., the sum of P_{gr} and P_w) is greater than the total load demand P_{lr}. Consequently, the HVDC system transfers the surplus power P_{dcr} to the receiving-end grid. Apart from these general conditions, no restriction or requirement is imposed on the WF. Therefore, for simplicity, the WF has been modeled as an intermittent power source [27]. Similarly, the accumulated dynamic response of the generators on each-side grid is represented by a second-order transfer function [28].

The reference signals of the HVDC system consist of two components, corresponding to PFC and SFC, as in the case of a common GFR scheme for generators. The PFC is achieved using droop controllers with coefficients of $R_{i(r)}$ and $K_{i(r)}$. Active power sharing between the HVDC converters and generators is achieved using controllers with $R_{i(r)}$, so that $\Delta f_{i(r)}$ can be stabilized in a localized manner. Similarly, using controllers with $K_{i(r)}$, ΔV_{dc} is stabilized via dc power sharing between the HVDC converters. The inertial responses are also emulated using derivative controllers to further exploit the fast dynamics of the HVDC converters.

The PFC support of an HVDC converter acts as a disturbance in the ac grid interfaced with the other converter. For example, f_i decreases for an increase in P_{li}, activating the droop controller with R_i. This increases P_{dci} and, consequently, P_{dcr} (see (24) and (25)), leading to a decrease in f_r. Furthermore, the frequency deviation leads to conflict between the droop controllers. Specifically, for $\Delta f_r < 0$, the controller with R_r is then activated to reduce P_{dcr} and hence P_{dci}, whereas the controller with R_i would still attempt to increase P_{dci} to stabilize f_i. Moreover, as the reduction in P_{dcr} is achieved by decreasing V_{dcr_ref}, the controllers with K_r and K_i are activated to increase P_{dcr} and decrease P_{dci}, respectively. In other words, dc power sharing degrades the PFC support of the controllers with R_r and R_i. Similarly, Δf_i resulting from ΔP_{lr} causes conflicts in the operations of the localized, droop controllers. Given the droop control characteristics, an LQG controller is designed for the coordinated SFC of ΔV_{dcr} and ΔI_{dci} for the HVDC system and ΔP_{gr} and ΔP_{gi} for the generators, as discussed in Section III, restoring f_i, f_r, and V_{dc} to their nominal values.

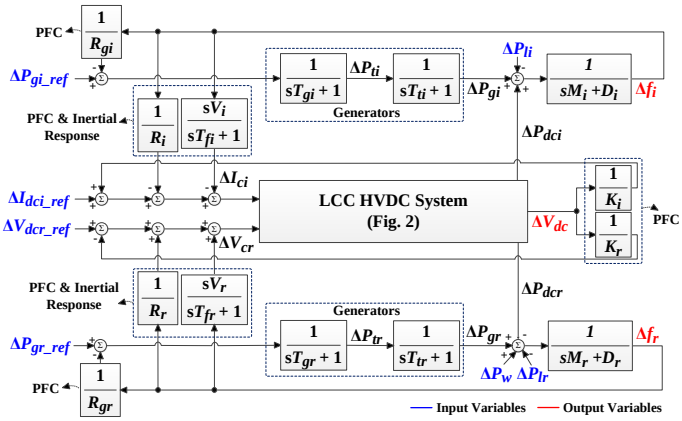

Fig. 3. Proposed GFR support by the HVDC system via inertia emulation, PFC, and SFC with variation in the load demands and WF power generation.

III. Design and Analysis of an LQG Controller For Optimal SFC of LCC HVDC System

A. Design of an LQG Controller for Optimal SFC

The small-signal model of the HVDC system and generators, shown in Fig. 3, can be represented in state space form as:

$$d\mathbf{X}(t)/dt = \mathbf{A}\cdot\mathbf{X}(t) + \mathbf{B}_\mathbf{r}\cdot\mathbf{r}(t) + \mathbf{B}_\mathbf{w}\cdot\mathbf{w}(t), \tag{26}$$

$$\mathbf{Y}(t) = \mathbf{C}\cdot\mathbf{X}(t), \tag{27}$$

with the states, inputs, and outputs arranged, respectively, as:

$$\mathbf{X}(t) = [\Delta f_i,\ \Delta P_{gi},\ \Delta P_{ti},\ \Delta I_{ci},\ \Delta I_{dci},\ \Delta f_r,\ \Delta P_{gr},\ \Delta P_{tr},\ \Delta V_{cr},\ \Delta V_{dcr},\ \Delta V_{drop}]^T, \tag{28}$$

$$\mathbf{r}(t) = [\Delta P_{gi\_ref},\ \Delta P_{gr\_ref},\ \Delta I_{dci\_ref},\ \Delta V_{dcr\_ref}]^T, \tag{29}$$

$$\mathbf{w}(t) = [\Delta P_{li},\ \Delta P_{lr} - \Delta P_w]^T, \tag{30}$$

$$\mathbf{Y}(t) = \left[\Delta f_i,\ \Delta f_r,\ \Delta V_{dcr},\ \Delta V_{drop}\right]^T, \tag{31}$$

where $\mathbf{A}$, $\mathbf{B_r}$, $\mathbf{B_w}$, and $\mathbf{C}$ are presented in the Appendix. In (28), ΔV_{drop} is defined as $\Delta V_{dci} - \Delta V_{dcr}$.

For optimal SFC, (26) and (27) are augmented by integrating the integrals of $[\Delta f_i,\ \Delta f_r,\ \Delta V_{dcr},\ \Delta V_{drop}]^T$ with $\mathbf{X}(t)$ and $\mathbf{Y}(t)$ as:

$$\frac{d}{dt}\left[\int \Delta f_i dt \quad \int \Delta f_r dt \quad \int \Delta V_{dcr} dt \quad \int \Delta V_{drop} dt \quad \mathbf{X}(t)\right]^T = \tag{32}$$

$$\begin{bmatrix} [\mathbf{O}]_{4\times4} & \begin{matrix} 1 & [\mathbf{O}]_{1\times5} & [\mathbf{O}]_{1\times5} \\ [\mathbf{O}]_{1\times5} & 1 & [\mathbf{O}]_{1\times5} \\ [\mathbf{O}]_{1\times9} & 1 & 0 \\ [\mathbf{O}]_{1\times5} & [\mathbf{O}]_{1\times5} & 1 \end{matrix} \\ [\mathbf{O}]_{11\times4} & \mathbf{A} \end{bmatrix} \begin{bmatrix} \int \Delta f_i dt \\ \int \Delta f_r dt \\ \int \Delta V_{dcr} dt \\ \int \Delta V_{drop} dt \\ \mathbf{X}(t) \end{bmatrix} + \begin{bmatrix} \mathbf{O} \\ \mathbf{B}_\mathbf{r} \end{bmatrix} \mathbf{r}(t) + \begin{bmatrix} \mathbf{O} \\ \mathbf{B}_\mathbf{w} \end{bmatrix} \mathbf{w}(t),$$

$$\left[\mathbf{Y}(t),\ \int \Delta f_i\ dt,\ \int \Delta f_r\ dt,\ \int \Delta V_{dcr}\ dt,\ \int \Delta V_{drop}\ dt\right]^T = \tag{33}$$

$$\begin{bmatrix} [\mathbf{O}]_{4\times4} & \mathbf{C} \\ [\mathbf{I}]_{4\times4} & [\mathbf{O}]_{4\times11} \end{bmatrix} \cdot \left[\int \Delta f_i dt \quad \int \Delta f_r dt \quad \int \Delta V_{dcr} dt \quad \int \Delta V_{drop} dt \quad \mathbf{X}(t)\right]^T.$$

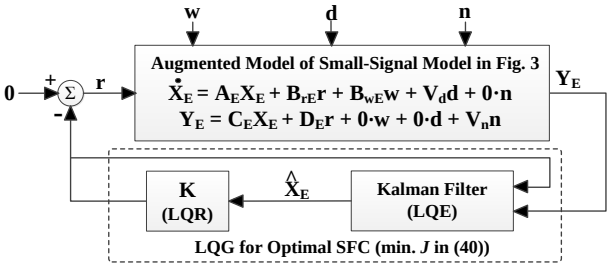

Fig. 4. An LQG controller integrated with the small-signal model (see Fig. 3) of the LCC HVDC system and conventional generators.

The augmented state-space model given by (32) and (33) can be represented in compact form as:

$$\frac{d}{dt}\mathbf{X}_E(t) = \mathbf{A}_E\cdot\mathbf{X}_E(t) + \mathbf{B}_{rE}\cdot\mathbf{r}(t) + \mathbf{B}_{wE}\cdot\mathbf{w}(t)\ , \tag{34}$$

$$\mathbf{Y}_E(t) = \mathbf{C}_E\cdot\mathbf{X}_E(t)\ , \tag{35}$$

where

$$\mathbf{X}_E(t) = \left[\int\Delta f_i\ dt,\ \int\Delta f_r\ dt,\ \int\Delta V_{dcr}\ dt,\ \int\Delta V_{drop}\ dt,\ \mathbf{X}(t)\right]^T, \tag{36}$$

$$\mathbf{Y}_E(t) = \left[\mathbf{Y}(t),\ \int\Delta f_i\ dt,\ \int\Delta f_r\ dt,\ \int\Delta V_{dcr}\ dt,\ \int\Delta V_{drop}\ dt\right]^T. \tag{37}$$

The augmented coefficient matrices are given as:

$$\mathbf{A}_E = \begin{bmatrix}\mathbf{O} & \mathbf{A}_s\\ \mathbf{O} & \mathbf{A}\end{bmatrix},\ \mathbf{B}_{rE} = \begin{bmatrix}\mathbf{O}\\ \mathbf{B}_r\end{bmatrix},\ \mathbf{B}_{wE} = \begin{bmatrix}\mathbf{O}\\ \mathbf{B}_w\end{bmatrix},\ \mathbf{C}_E = \begin{bmatrix}\mathbf{O} & \mathbf{C}\\ \mathbf{I} & \mathbf{O}\end{bmatrix}, \tag{38}$$

where

$$\mathbf{A}_s = \begin{bmatrix}1 & [\mathbf{O}]_{1\times5} & [\mathbf{O}]_{1\times5}\\ [\mathbf{O}]_{1\times5} & 1 & [\mathbf{O}]_{1\times5}\\ [\mathbf{O}]_{1\times9} & 1 & 0\\ [\mathbf{O}]_{1\times5} & [\mathbf{O}]_{1\times5} & 1\end{bmatrix}\ . \tag{39}$$

Moreover, communication time delays and measurement noise are reflected in the augmented model, as shown in Fig. 4; these are modeled as input and output disturbances $\mathbf{d}(t)$ and $\mathbf{n}(t)$, respectively, using normally distributed random variables.

As shown in Fig. 4, a state feedback controller $\mathbf{r}(t) = -\mathbf{K}\cdot\mathbf{X}_E(t)$ is integrated with the augmented model to minimize the maximum variations in f_i, f_r, and V_{dc}, while also restoring them to the nominal values in steady state. Considering the control efforts of the HVDC system and generators, a cost function for the feedback controller can be formulated as:

$$J = \int_0^\infty \left(\mathbf{X}_E(t)^T\cdot\mathbf{Q}\cdot\mathbf{X}_E(t) + \mathbf{r}(t)^T\cdot\mathbf{R}\cdot\mathbf{r}(t)\right) dt\ . \tag{40}$$

In (40), $\mathbf{Q}$ is a diagonal matrix with weighting coefficients, each of which is multiplied by the square of each state variable $\int\Delta f_i\ dt$, $\int\Delta f_r\ dt$, $\int\Delta V_{dcr}\ dt$, $\int\Delta V_{drop}\ dt$, Δf_i, Δf_r, ΔV_{dcr}, and ΔV_{drop}, in $\mathbf{X}_E(t)$. Similarly, $\mathbf{R}$ is a diagonal matrix with weighting coefficients for the squares of the input variables in $\mathbf{r}(t)$. Each coefficient in $\mathbf{Q}$ and $\mathbf{R}$ can be determined adaptively by considering the operating conditions of the HVDC system and interfacing grids. For example, by increasing the coefficients of terms related to ΔV_{dcr}, we can prevent excessive variation in the dc-link voltage and firing angle, while still improving the real-time GFR, as discussed in Section IV-E. For $\mathbf{Q}$ and $\mathbf{R}$, there is a matrix of $\mathbf{K} = \mathbf{R}^{-1}\cdot\mathbf{B}_r^T\cdot\mathbf{P}$ minimizing J in (40), such that $\mathbf{P}$ is the solution to:

$$\mathbf{A}_E^T\cdot\mathbf{P} + \mathbf{P}\cdot\mathbf{A}_E + \mathbf{Q} - \mathbf{P}\cdot\mathbf{B}\cdot\mathbf{R}^{-1}\cdot\mathbf{B}^T\cdot\mathbf{P} = \mathbf{O}. \tag{41}$$

To establish the optimal $\mathbf{r}(t)$, all states in $\mathbf{X}_E(t)$ need to be measurable. As shown in Fig. 4, a Kalman filter [29] is often adopted to estimate the unknown states, using the measured states or outputs $\mathbf{Y}_E(t)$: i.e.,

$$\mathbf{r}(t) = -\mathbf{K}\cdot\mathbf{X}_E(t) \approx -\mathbf{K}\cdot\hat{\mathbf{X}}_E(t)\ , \tag{42}$$

where $\hat{\mathbf{X}}_E$ is the estimate of $\mathbf{X}_E$. Given the successful performance of the Kalman filter (i.e., $\hat{\mathbf{X}}_E \approx \mathbf{X}_E$), the transfer function matrix $\mathbf{V}(s)$ between $\mathbf{w}(s)$ and $\mathbf{Y}_E(s)$ of the complete state-space model, shown in Fig. 4, is obtained as:

$$\mathbf{Y}_E(s) = \mathbf{V}(s)\cdot\mathbf{w}(s) = \mathbf{C}_E\left[s\mathbf{I} - \left(\mathbf{A}_E - \mathbf{B}_{rE}\mathbf{K}\right)\right]^{-1}\mathbf{B}_{wE}\cdot\mathbf{w}(s)\ , \tag{43}$$

or, equivalently,

$$\begin{bmatrix}\Delta f_i(s)\\ \Delta f_r(s)\\ \vdots\end{bmatrix} = \begin{bmatrix}V_{11}(s) & V_{12}(s)\\ V_{21}(s) & V_{22}(s)\\ \vdots & \vdots\end{bmatrix}\begin{bmatrix}\Delta P_{li}(s)\\ \Delta P_{lr}(s) - \Delta P_w(s)\end{bmatrix}\ . \tag{44}$$

B. Eigenvalue Analysis of the Proposed GFR Support

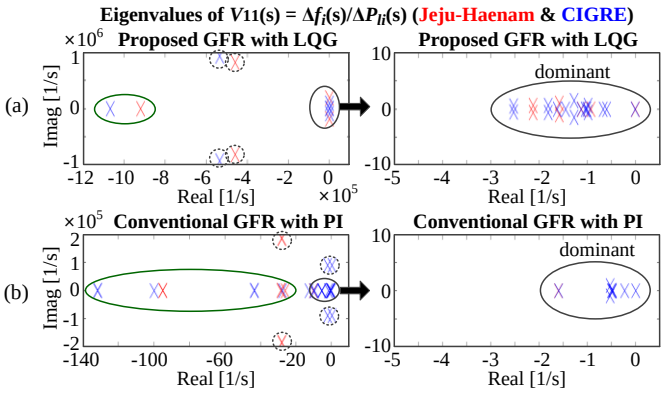

Fig. 5. Eigenvalues of $\Delta f_i/\Delta P_{li}$: (a) proposed and (b) conventional GFR.

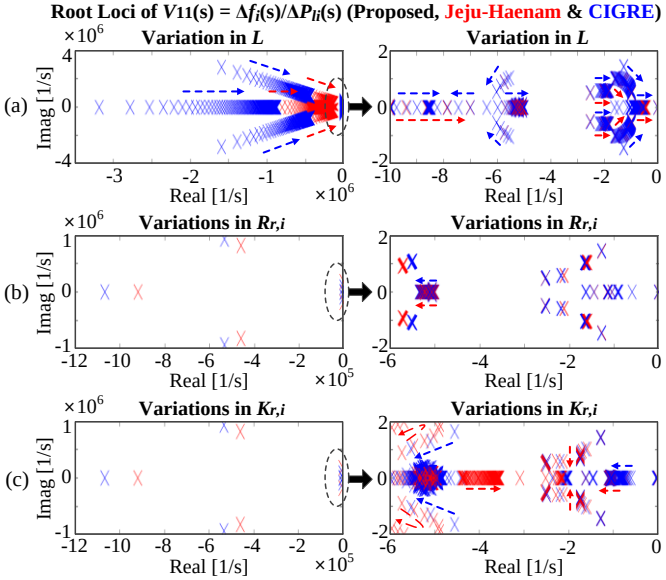

Fig. 6. Root loci of $\Delta f_i/\Delta P_{li}$ in the proposed strategy for increasing (a) L from 4.4×10^{-5} pu to 4.4×10^{-3} pu and (b) $R_{i(r)}$ and (c) $K_{i(r)}$ from 0.1 to 10.0.

Using (44), eigenvalue analysis is performed for two types of LCC HVDC system (i.e., the Jeju-Haenam system [20] and the CIGRE benchmark system [21]), focusing on the frequency deviations for the load demand variations: i.e., $\Delta P_w(s) = 0$. Fig. 5 shows the eigenvalues of $\Delta f_i(s)/\Delta P_{li}(s)$ for the proposed and conventional GFR strategies, where the LQG and PI controllers,

respectively, are adopted for the SFC of the HVDC system and generators. For both strategies, the eigenvalues are the same as those of $\Delta f_i(s)/\Delta P_{lr}(s)$, $\Delta f_r(s)/\Delta P_{lr}(s)$, and $\Delta f_r(s)/\Delta P_{li}(s)$.

Specifically, Fig. 5(a) shows that, with the proposed strategy, both types of HVDC system have three groups of poles: i.e., (Group A) the poles located far from the imaginary axis; (Group B) the complex conjugate poles with large imaginary values; and (Group C) the poles placed close to the imaginary axis. In Groups A to C, the poles are encircled by the green line, black dotted lines, and black line, respectively. In this paper, Group C has been defined as the dominant poles; the most dominant pole is not specified, because all poles of Group C significantly affect the dynamic responses of the HVDC system and the interfacing grids. Similarly, Fig. 5(b) shows that, with the conventional strategy, the dominant poles lie in the *s*-plane with the real and imaginary axes ranging from –5 to 0 and from –10 to 10, respectively, as in the proposed strategy. This allows for a fair comparison between the proposed and conventional strategies. For both HVDC systems, the dominant poles and complex-conjugate poles with large imaginary values are located further away from the imaginary axis with the proposed strategy than with the conventional strategy. This indicates that, in the proposed strategy, f_i can be restored to the nominal value with a faster response time and smaller oscillations.

In addition, Fig. 6 shows the root loci of $\Delta f_i(s)/\Delta P_{li}(s)$ in the proposed GFR strategy when the dc-link parameters and controller gains of the HVDC system vary. Root locus analysis explores the performance of the proposed strategy applied to various HVDC units differing in terms of both parameters and gains, confirming that the strategy is widely applicable. Note that the root locus consists of the poles obtained using different optimal values of **K** for each set of (L, R, C, R_i, R_r, K_i, K_r). Specifically, the dc-link parameters L, R, and C increase from 4.4×10^{-5} to 4.4×10^{-3} pu, from 4.4×10^{-4} to 4.4×10^{-2} pu, and from 1.1×10^{-8} to 8.8×10^{-7} pu, respectively [30], [31]; the ranges have been determined based on the dc-link parameters of common HVDC systems [31]–[33]. Moreover, the droop coefficients, $R_{i(r)}$ and $K_{i(r)}$, increase from 0.1 to 10.0. The wider the ranges of the parameters, the more thorough and complete the analysis.

In Fig. 6(a), as L increases, the poles move towards the imaginary axis in both types of HVDC system, thus decreasing the damping ratio and increasing the settling time of the closed-loop system (i.e., Fig. 4). Then, Δf_i caused by ΔP_{li} becomes more persistent, returning to zero after longer time delays. In other words, the HVDC system responds more slowly to reference signals delivered by the grid- and converter-level controllers, thus contributing little to real-time GFR in interfacing grids. Therefore, for real-time GFR support, dc link and dc harmonic filters with low inductance are preferred to move the real and complex-conjugate poles away from the imaginary axis. Note that if the inductance is too low, the dc filters are not effective and the HVDC system becomes highly sensitive to internal and external disturbances. On the other hand, if the inductance is too high, the HVDC system operation is likely to become unstable with large oscillations in the transferred power. For brevity, the root loci of the variations in R and C are not provided, because the variations only marginally affect the eigenvalues. Fig. 6(b) and (c) also show that, as $R_{i(r)}$ and $K_{i(r)}$ increase, the dominant poles on the real axis move away from the imaginary axis for both types of system. This indicates that the droop controllers of the HVDC converters, discussed in Section II-B, are well coordinated, stabilizing the frequency successfully within a short period after the load disturbance.

IV. Case Studies and Results

A. Test System and Simulation Conditions

TABLE II. Parameters for the Case Studies

Devices	Description	Parameters	Values
Jeju-Haenam HVDC system	Nominal dc voltages	V_{dcr0}, V_{dci0} [kV]	184.0, 183.5
	Nominal dc currents	I_{dcr0}, I_{dci0} [A]	407.6
	HVDC-link parameters	R [Ω], L [H], C [μF]	1.116, 0.2, 54
	Converter reactance	X_{cr}, X_{ci} [Ω]	7.99
	Converter overlap angles	μ_{r0}, μ_{i0} [°]	2.44
	Firing and extinction angles	α_0, γ_0 [°]	15.0, 18.0
	TR secondary voltages	V_{lr}, V_{li} [kV]	75.9, 82.2
	TR tap ratios	TR_r, TR_i	0.9
	Voltage controller gains	k_{pr}, k_{ir}	5.5, 20.1
	Current controller gains	k_{pi}, k_{ii}	0.001, 10.0
	Number of bridges	N	2
	Time constants of HVDC converters and the dc link	$T_{r(i)}$, T_k, $T_{fr(i)}$	0.02, 0.001, 0.1
	Time constants of dc filters	T_{dcf1}, T_{dcf2}	0.01, 0.08
Generators in ac grids	Inertia and damping	M_r, M_i, D_i, D_r	5, 5, 1, 1
	Time constants	T_{gr}, T_{gi}, T_{tr}, T_{ti}	0.2, 0.2, 0.5, 0.5
PFC	Emulated inertia	V_r, V_i	5
	Droop gains (HVDC)	K_r, K_i, R_r, R_i	0.5
	Droop gains (Gen.)	R_{gr}, R_{gi}	0.5
SFC (Conv.)	PI gains (HVDC)	KP_r, KP_i, KI_r, KI_i	9, 9, 6, 6
	PI gains (Gen.)	KP_r, KP_i, KI_r, KI_i	9, 9, 6, 6

TABLE III. Features of the Proposed and Conventional Strategies

HVDC control strategies		ΔV_{dc}	GFR	SFC
Proposed	Case 1	time-varying	both-side grids	LQG
Conventional	Case 2	time-varying	both-side grids	PI
	Case 3	fixed	inverter-side grid	PI

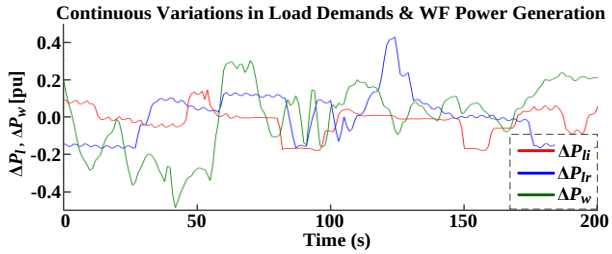

Fig. 7. Continuous variations in load demands and wind power generation.

The proposed optimal control strategy was tested using the parameter sets and operating conditions of two HVDC systems: the Jeju-Haenam system [20], [34] and the CIGRE benchmark system [21]. The Jeju-Haenam system has a rated power of 150 MW and a rated voltage of 184 kV. It delivers surplus power generated at the rectifier terminal of the Haenam grid to the inverter terminal of the Jeju grid via a 100-km dc cable. The Jeju grid is weaker than the Haenam grid; the short-circuit ratios of the Jeju and Haenam grids are 4.0 and 14.4, respectively [35], [36]. The HVDC converters operate with both constant and time-varying power references under normal conditions. Each converter includes a converter transformer, 12 thyristor valves, and internal controllers that regulate the firing or extinction angles. Table II lists the real parameters of the Jeju-Haenam system [17], [37] and the model parameters of the non-reheat turbine generators [28] in the rectifier- and

inverter-side grids. It also shows the coefficients for the emulated inertial responses and droop controllers, as well as the PI controllers for the conventional strategy. The real and benchmark HVDC systems were comprehensively modeled in MATLAB/SIMULINK using averaged circuit models of the converters, detailed models of the dc link and converter transformers, and grid- and converter-level controllers with nonlinear signal processing capabilities. The comprehensive model was used to validate the small-signal model and hence the proposed strategy.

Table III shows the main features of the proposed (Case 1) and conventional (Cases 2 and 3) strategies. The comparison between Cases 1 and 2 was taken into account to analyze the effect of the proposed LQG controller on the real-time GFR, given the operating characteristics of the droop controllers, discussed in Sections II-B and III-A. Moreover, Case 3 represents a common condition of the HVDC system [6], [8] to support only the inverter-side GFR: i.e., no feedback loops with $1/R_r$, $s{\cdot}V_r$, K_r, and K_i. We compared Case 1 and Case 3 to analyze the effectiveness of the proposed dc voltage control for improving the GFR on both rectifier and inverter sides. Note that in Cases 1–3, the control input of I_{dci_ref} is integrated with the feedback loops for the inertia emulation, PFC, and SFC. This allows for a fair comparison between the proposed and conventional strategies in terms of the optimal time-varying control of V_{dcr}, which is the main focus of this paper. Due to the inertia emulation, the fast response of the inverter can be successfully exploited in Cases 1–3, increasing or decreasing I_{dci} almost instantaneously after load disturbance. Fig. 7 shows the variations in load demands ΔP_{li} and ΔP_{lr}, reflecting the scaled-up RegD signals [38] over a time period of 200 s. It also shows the intermittent power generation ΔP_w of the WF. In addition to these profiles, stepwise variations in ΔP_{li} and ΔP_{lr} were considered to evaluate the performance of the GFR support provided by the HVDC system.

B. Validating the Small-Signal Model of the HVDC System

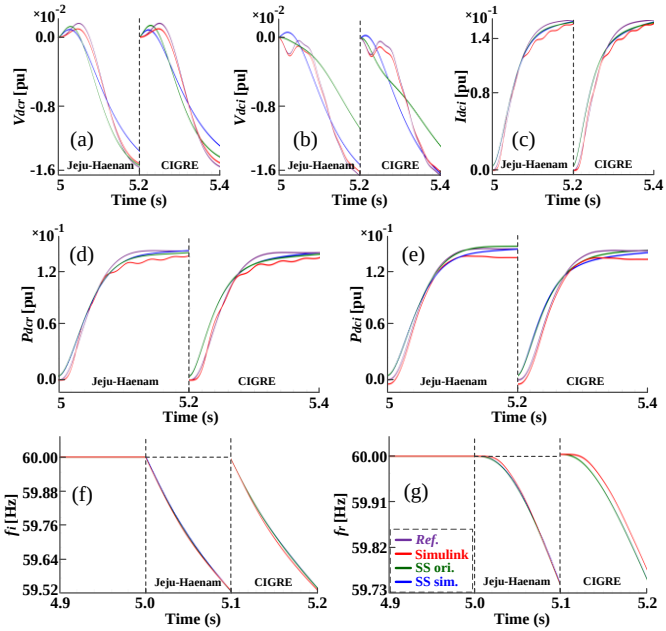

Fig. 8. Close-up plots of the step responses to ΔP_{li} (t) = 0.3 pu for the proposed strategy: (a) V_{dcr}, (b) V_{dci}, (c) I_{dci}, (d) P_{dcr}, (e) P_{dci}, (f) f_i, and (g) f_r.

We compared the transient responses of the small-signal models and the comprehensive SIMULINK model, discussed in Sections II-A and IV-A, respectively, for both types of HVDC system to a step variation in P_{li} of 0.3 pu. Fig. 8(a)–(c) show that, for both types, the transient responses of the three models were similar to each other for each profile of V_{dcr}, V_{dci}, and I_{dci}, respectively. This also led to good consistency between the simplified small-signal model and the other models for each profile of P_{dcr} and P_{dci} and, consequently, of f_r, and f_i, as shown in Fig. 8(d)–(g), respectively. The simplified model reflected well the HVDC system operation when $L \le 5$ H and $C \le 500$ μF. In general, the L and C of real HVDC systems are considerably smaller than 5 H and 500 μF, respectively [31]–[33]. This implies that conversion from the original small-signal model to the simplified model is valid under common practical operating conditions of HVDC systems, confirming the accuracy of the case study results obtained using the simplified model presented in Sections IV-C, D, and E.

C. Comparisons of Stepwise Load Demand Variations

Fig. 9 shows f_i, f_r, V_{dc}, and I_{dc} for the step responses of the Jeju-Haenam HVDC system to ΔP_{li} and ΔP_{lr}, which increased by 0.3 pu at t = 5 s and 35 s, respectively, over 15 s. As indicated in Table IV, the proposed strategy (i.e., Case 1) decreased the sum of the maximum deviations of f_i and f_r (i.e., $|\Delta f_i|_{\max}+|\Delta f_r|_{\max}$) by 28.8% and 21.8%, compared to the conventional strategies (i.e., Cases 2 and 3, respectively), while resulting in a maximum variation in the dc-link voltage of only 4.3%. Moreover, in Case 1, f_i and f_r were restored back to the nominal value more rapidly, and with smaller overshooting than in Cases 2 and 3.

Fig. 10 shows the variations in α and γ for the optimal profiles of V_{dc} and I_{dc}. In Case 1, the decreases in f_i and f_r at t = 5 s activated the inertia emulation (with gains of V_i and V_r) and the frequency-power droop control (with gains of R_i and R_r) of the HVDC converters. This decreased V_{dcr_ref} and increased I_{dci_ref}, triggering rapid increases in both α and γ at t = 5 s. The reduction in V_{dcr_ref} (and hence V_{dc}) activated the dc voltage-power droop control (with gains of K_i and K_r), thus increasing V_{dcr_ref} and decreasing I_{dci_ref} towards the nominal values. Therefore, α and γ were reduced after reaching peak values of 16.1° and 21.0°, respectively. Due to the SFC, V_{dcr} and α were restored to their initial values. On the other hand, I_{dc} and γ remained at 464.7 A and 19.5°, respectively, continuously compensating for the increase in P_{li}. On the contrary, in Case 2, I_{dc} and γ were restored to their initial values at approximately t = 12 s. This shows that the conventional SFC with PI controllers uses only the inverter-side generators to compensate for variations in P_{li}. In Case 3, V_{dcr} and α remained at their initial values, implying that the HVDC system and inverter-side generators did not contribute to rectifier-side GFR. A comparative analysis of the α- and γ-profiles was also performed when P_{lr} increased at t = 35 s. Both α and γ were maintained within acceptable ranges (i.e., $5° \le \alpha \le 135°$ and $5° \le \gamma \le 90°$ [37]). This confirms that the proposed strategy ensures normal operation (i.e., not a saturated response) of HVDC converters.

Fig. 11 represents the corresponding profiles of ΔP_{dci}, ΔP_{gi}, and ΔP_{gr}. In Case 1, ΔP_{gi} and ΔP_{gr} increased by 0.15 pu (or,

more accurately, by 0.16 pu and 0.14 pu, respectively) when ΔP_{li} or ΔP_{lr} increased by 0.30 pu, given the identical model parameters and controller gains of the rectifier- and inverter-side generators. In other words, the LQG controller enabled the load demand variation to be shared between the generators in both-side grids, reducing frequency deviation. Optimal control

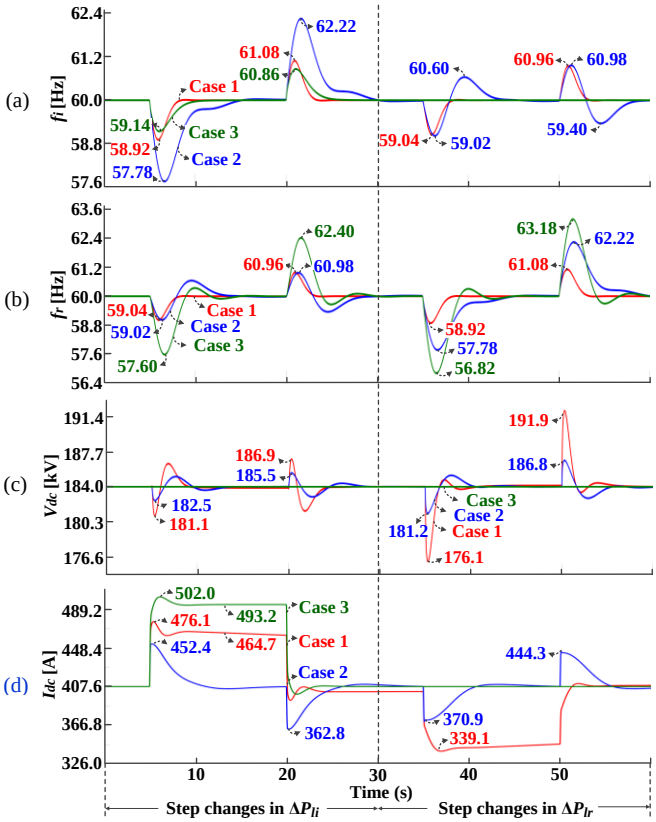

Fig. 9. Step responses to ΔP_{li} ($t = 5^+$ s) = ΔP_{lr} ($t = 35^+$ s) = 0.3 pu over 15 s with the proposed and conventional strategies: (a) f_i, (b) f_r, (c) V_{dc}, and (d) I_{dc}.

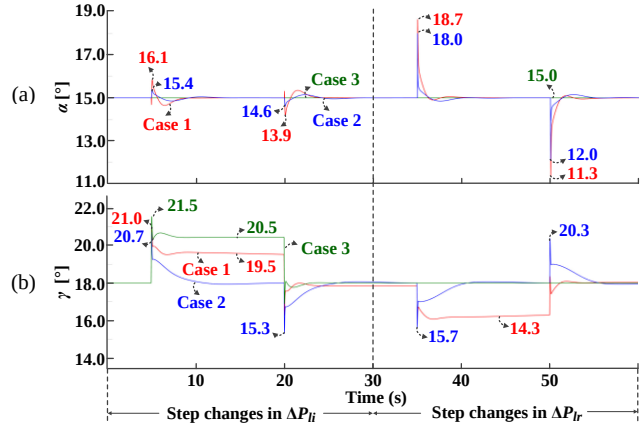

Fig. 10. Corresponding variations in the (a) firing and (b) extinction angles.

TABLE IV. COMPARISONS OF THE STEP RESPONSE TEST RESULTS

Maximum variations	Case 1		Case 2		Case 3	
	Individual	Total	Individual	Total	Individual	Total
$\lvert\Delta f_i\rvert_{max}$ [Hz]	1.08	3.16	2.22	4.44	0.86	4.04
$\lvert\Delta f_r\rvert_{max}$ [Hz]	1.08		2.22		3.18	
$\lvert\Delta P_{dci}\rvert_{max}$ [pu]	0.17	0.34	0.10	0.20	0.23	0.46
$\lvert\Delta P_{dcr}\rvert_{max}$ [pu]	0.17		0.10		0.23	
$\lvert\Delta P_{gi}\rvert_{max}$ [pu]	0.20	0.39	0.32	0.63	0.10	0.51
$\lvert\Delta P_{gr}\rvert_{max}$ [pu]	0.19		0.31		0.41	

of the dc-link voltage and current was also achieved to transfer the increased power generation in both the transient and steady state. In contrast, the PI controllers in Case 2 caused the generators to compensate for the load variations that occurred principally on the same side of the HVDC system. For ΔP_{li} ($t = 5^+$ s) = 0.30 pu, ΔP_{gr} initially increased by 0.10 pu and then remained close to zero. Therefore, the HVDC system could only marginally contribute to the rectifier-side GFR, and only during the period of the transient state, resulting in larger deviations and overshooting of f_i and f_r. In Case 3, ΔP_{li} ($t = 5^+$ s) = 0.3 pu caused larger variations in P_{gr} and f_r than in P_{gi} and f_i, which can be problematic when the rectifier-side grid includes critical loads and generators with limited capacities. For all cases, ΔP_{dci} and ΔP_{dcr} changed faster than ΔP_{gi} and ΔP_{gr}. This verifies the effectiveness of the inertia emulation and droop control in exploiting the fast response of the HVDC converters.

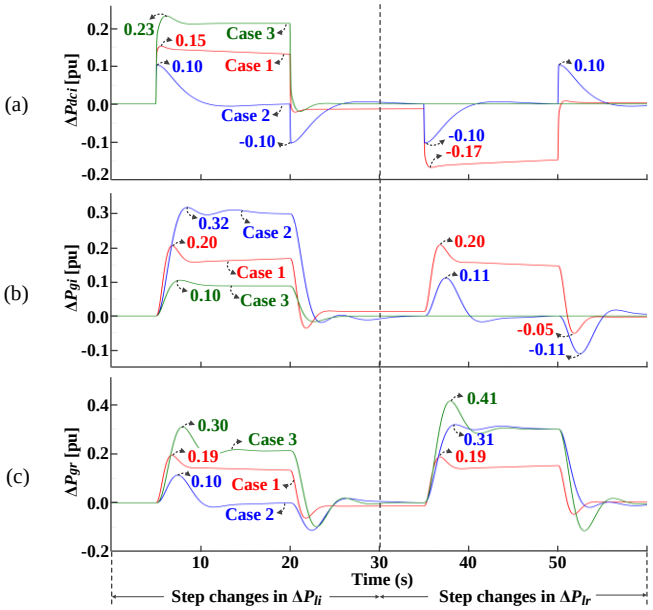

Fig. 11. Corresponding variations in the transferred and generated power: (a) ΔP_{dci}, (b) ΔP_{gi}, and (c) ΔP_{gr}.

D. Comparisons of Continuous Load Demand Variations

Additional case studies performed when ΔP_{li}, ΔP_{lr}, and ΔP_w varied continuously, as shown in Fig. 7. Fig. 12 shows the corresponding profiles of f_i, f_r, V_{dc}, and I_{dc}, and Fig. 13 represents the profiles of α and γ. In Case 1, both V_{dc} and I_{dc} (and, consequently, α and γ) exhibited more rapid and larger variations than Cases 2 and 3. In other words, the proposed strategy enables more active and adaptive control of the HVDC system, further reducing Δf and ΔP_g in both-side grids. Note that ΔV_{dc}, $\Delta\alpha$, and $\Delta\gamma$ were maintained within acceptable ranges; the maximum variations were 2.5%, 0.7°, and 2.9°, respectively.

Table V lists the rms variations of Δf and ΔP_g, which were estimated as:

$$\Delta f_{rms} = \left(\sum_{m=1}^{M} \Delta f_m^2 / M\right)^{1/2} \quad \text{and} \quad \Delta P_{g,rms} = \left(\sum_{m=1}^{M} \Delta P_{g,m}^2 / M\right)^{1/2}, \quad (45)$$

where m is the index of the measurement sample and M is the total number of samples. In Case 1, the sum of $\Delta f_{i,rms}$ and $\Delta f_{r,rms}$ decreased by 57.3 % and 53.1%, compared to Cases 2 and 3, respectively, verifying the effectiveness of the proposed control

strategy in improving the GFR in both rectifier- and inverter-side networks. In Case 1, $\Delta P_{g,rms}$ was 23.3% and 8.0% smaller than those in Cases 2 and 3, respectively, because the total variation in the load demand and WF power generation was shared among all generators on both sides. This implies that the proposed strategy can mitigate the operational requirements (e.g., the spinning reserve capacity) of the generators.

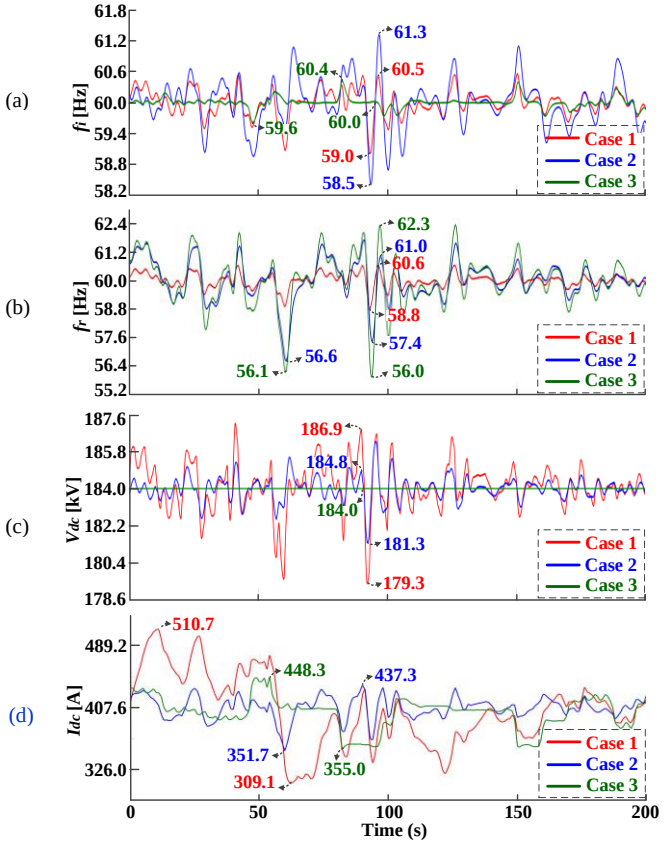

Fig. 12. Responses to continuous variations in ΔP_{li}, ΔP_{lr}, and ΔP_w for the proposed and conventional strategies: (a) f_i, (b) f_r, (c) V_{dc}, and (d) I_{dc}.

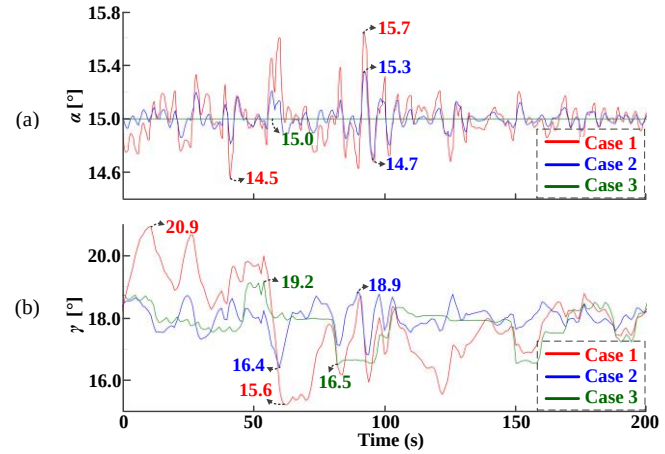

Fig. 13. Corresponding variations in the (a) firing and (b) extinction angles.

TABLE V. COMPARISONS OF THE CONTINUOUS RESPONSE TEST RESULTS

Δf_{rms} and ΔP_{rms}	Case 1		Case 2		Case 3	
	Individual	Total	Individual	Total	Individual	Total
$\Delta f_{i,rms}$ [Hz]	0.25	0.53	0.44	1.24	0.10	1.13
$\Delta f_{r,rms}$ [Hz]	0.28		0.80		1.03	
$\Delta P_{gi,rms}$ [pu]	0.11	0.23	0.08	0.30	0.02	0.25
$\Delta P_{gr,rms}$ [pu]	0.12		0.22		0.23	

E. Proposed Strategy Performance under Various Conditions

TABLE VI. STEP RESPONSES FOR DIFFERENT VALUES OF LQG PARAMETER **Q**

Frequency [Hz]			HVDC-link voltage [kV]	
$\lvert\Delta f_i\rvert_{max}$	$\lvert\Delta f_r\rvert_{max}$	Total	$\lvert\Delta V_{dc}\rvert_{max}$ for ΔP_{li}	$\lvert\Delta V_{dc}\rvert_{max}$ for ΔP_{lr}
0.96	0.96	1.92	0.7	2.0

Transferred power [pu]			Generated power [pu]		
$\lvert\Delta P_{dci}\rvert_{max}$	$\lvert\Delta P_{dcr}\rvert_{max}$	Total	$\lvert\Delta P_{gi}\rvert_{max}$	$\lvert\Delta P_{gr}\rvert_{max}$	Total
0.16	0.16	0.32	0.18	0.16	0.34

TABLE VII. CONTINUOUS RESPONSE RESULTS UNDER DIFFERENT INERTIAL RESPONSE AND DROOP CONTROL CONDITIONS

	Δf_{rms} and ΔP_{rms}	Case 1		Case 2		Case 3	
		Individual	Total	Individual	Total	Individual	Total
a	$\Delta f_{i\,rms}$ [Hz]	0.24	0.52	0.53	1.47	0.11	1.14
	$\Delta f_{r\,rms}$ [Hz]	0.28		0.94		1.03	
	$\Delta P_{gi\,rms}$ [pu]	0.11	0.23	0.09	0.32	0.02	0.25
	$\Delta P_{gr\,rms}$ [pu]	0.12		0.23		0.23	
b	$\Delta f_{i\,rms}$ [Hz]	0.25	0.53	0.37	1.38	0.10	1.13
	$\Delta f_{r\,rms}$ [Hz]	0.28		1.01		1.03	
	$\Delta P_{gi\,rms}$ [pu]	0.11	0.23	0.08	0.31	0.02	0.25
	$\Delta P_{gr\,rms}$ [pu]	0.12		0.23		0.23	

a: no droop control, b: no inertia emulation and no droop control

TABLE VIII. CONTINUOUS RESPONSE RESULTS FOR THE BENCHMARK MODEL

Δf_{rms} and ΔP_{rms}	Case 1		Case 2		Case 3	
	Individual	Total	Individual	Total	Individual	Total
$\Delta f_{i,rms}$ [Hz]	0.24	0.51	0.44	1.24	0.07	1.11
$\Delta f_{r,rms}$ [Hz]	0.27		0.80		1.04	
$\Delta P_{gi,rms}$ [pu]	0.11	0.23	0.08	0.30	0.02	0.25
$\Delta P_{gr,rms}$ [pu]	0.12		0.22		0.23	

TABLE IX. STEP RESPONSE RESULTS FOR THE BELO MONTE HVDC SYSTEM

Maximum variations	Case 1		Case 2		Case 3	
	Individual	Total	Individual	Total	Individual	Total
$\lvert\Delta f_i\rvert_{max}$ [Hz]	1.26	2.22	2.40	4.56	0.86	4.04
$\lvert\Delta f_r\rvert_{max}$ [Hz]	0.96		2.16		3.18	
$\lvert\Delta V_{dc}\rvert_{max}$ [kV]	29.6 (3.7×10^{-2} pu)		11.2 (1.4×10^{-2} pu)		0.0 (0.0 pu)	

TABLE X. CONTINUOUS RESPONSE RESULTS FOR THE BELO MONTE MODEL

Maximum variations	Case 1		Case 2		Case 3	
	Individual	Total	Individual	Total	Individual	Total
$\Delta f_{i,rms}$ [Hz]	0.24	0.49	0.42	1.22	0.10	1.13
$\Delta f_{r,rms}$ [Hz]	0.25		0.80		1.03	
$\Delta V_{dc,rms}$ [kV]	6.8 (8.5×10^{-3} pu)		2.3 (2.9×10^{-3} pu)		0.0 (0.0 pu)	

The case studies discussed in Section IV-C were repeated to analyze the performance of the proposed strategy using different values of the LQG parameters, particularly the weighting coefficients of **Q** (see (40)). Table VI shows the results of the step response test of the HVDC system when the weighting coefficients were increased 10-fold compared to the original values used in Section IV-C. The proposed strategy decreased the variation in both frequency and dc-link voltage, thereby enhancing the transient stability of both the HVDC system and the interfacing grids. Moreover, when we increased the weighting coefficients assigned to states Δf_i and Δf_r in $\mathbf{X_E}(t)$, the maximum frequency deviation gradually decreased. This implies that the proposed strategy allows the HVDC system to support the rectifier-side GFR more intensively than the inverter-side GFR, or vice versa, depending on the wind generation capacity and load composition, for example.

In addition, the case studies in Section IV-D were repeated to analyze the performance of the proposed strategy compared to the conventional strategies, under various inertia emulation and droop control conditions. Table VII shows the corresponding results. Moreover, the case studies were carried out using the CIGRE benchmark model [21] with a rated power of 1,000 MW and a rated voltage of 500 kV; Table VIII shows the numerical results. The proposed strategy was also tested using the Belo Monte HVDC system [39], which has a long transmission line with an equivalent inductance of 1,892 mH, which is approximately 9.46- and 3.17-fold those of the Jeju-Haenam and CIGRE systems, respectively. Tables IX and X summarize the case study results with respect to Δf_i, Δf_r, and ΔV_{dc} for the step and continuous response tests, respectively.

Under all conditions, the proposed strategy successfully reduced frequency deviations by optimally coordinating the HVDC converters and generators, resulting in relatively small variations in the dc-link voltage. The case study results also confirm that the effectiveness of the proposed strategy is attributable to the inherent capability of HVDC converters to respond faster than conventional generators, rather than the inductance itself of the dc link and dc harmonic filters.

F. Relative Lifetime Analysis of the Proposed Strategy

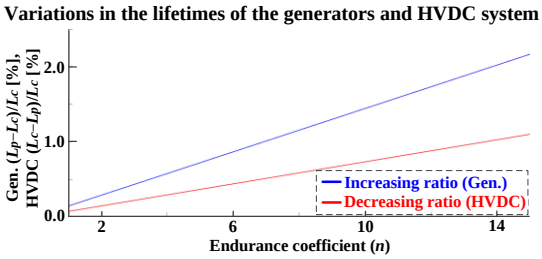

Fig. 14. Increasing and decreasing lifetime ratios of the generators and HVDC system, respectively, for Case 1 and Case 3.

In this paper, an inverse power modeling (IPM) method [40]–[42] was used to estimate the lifetimes of the HVDC system and generators when the proposed and conventional strategies were applied. In particular, ΔV_{dc}, Δf_i, and Δf_r were considered for lifetime estimation, because both strategies only marginally affect the ac voltage and the dc link has a zero-frequency voltage and current. Consequently, the IPM methods for the HVDC system and generators were established as:

$$\frac{L_{P,HVDC}}{L_{C,HVDC}} = \left(\frac{V_{dc,rms,P}}{V_{dc,rms,C}}\right)^{-n_V} \text{ and } \frac{L_{P,Gen}}{L_{C,Gen}} = \left(\frac{f_{i,rms,P} + f_{r,rms,P}}{f_{i,rms,C} + f_{r,rms,C}}\right)^{-n_f}, \quad (46)$$

where L_P and L_C are the lifetimes of the proposed and conventional strategies, respectively. In (46), n_V and n_f are the endurance coefficients for ΔV_{dc} and Δf, respectively. For simplicity, n_V and n_f were set to be equal (i.e., $n_V = n_f = n$) and were varied from 1 to 15 [40]–[42]. The IPM methods were applied to the case study results shown in Fig. 12. In Fig. 14, the red line indicates the decreasing ratio [i.e., $(L_{C,HVDC}–L_{P,HVDC})/L_{C,HVDC}$] of the lifetime of the HVDC system for Case 1 to that for Case 3 over the value of n. Similarly, the blue line represents the increasing ratio [i.e., $(L_{P,Gen}–L_{C,Gen})/L_{C,Gen}$] of the lifetime of the generators for Case 1 to that for Case 3. Note that, for the conventional strategies, the values of $(\Delta f_{i,rms} + \Delta f_{r,rms})$ and $\Delta V_{dc,rms}$ in Case 3 are lower than those in Case 2. Fig. 14 shows that the increasing ratios were greater than the decreasing ratios. This implies that the costs imposed by an increase in voltage insulation stress on the HVDC system can be sufficiently compensated by the savings attributable to reduced operating stress on the generators.

V. Conclusions

This paper has proposed a new control strategy for an LCC HVDC system, in which the dc-link voltage and current were optimally regulated to improve the GFR in both the rectifier- and inverter-side networks under normal operating conditions. A new small-signal model of an HVDC system was developed, verified via comparison with a comprehensive model, and integrated with feedback loops for inertia emulation and droop control. An LQG controller including a Kalman filter was also designed for optimal SFC while mitigating conflict between the droop controllers of the HVDC converters. An eigenvalue analysis was then conducted, focusing on the effects of the dc-link parameters and droop coefficients on the performance of the proposed strategy. Case studies were also carried out using models of a real LCC HVDC system and a CIGRE benchmark system, where the proposed strategy decreased the maximum frequency variation by 28.8% and the rms variation by 57.3% for stepwise and continuous load demand variations, respectively, compared to the conventional strategies. The proposed strategy enabled the total load demand variation to be shared between the generators in both-side grids, reducing the power generation variation by 23.3%. The proposed strategy was effective under various conditions of the LQG parameters, the system specifications, and the inertia emulation and droop control approaches. Further work will focus on the analysis of the proposed strategy under abnormal, contingent conditions of the HVDC system and ac networks (e.g., generator tripping, short-circuit faults, and commutation failures) to ensure frequency and voltage stability during and after contingency.

Appendix

The coefficients used in (5)–(18) are defined as:

$$a_{1x} = 3\sqrt{2}NV_{lx}\left(\pi TR_x\right)^{-1},\ a_{2x} = 3X_{cx}N\pi^{-1},\ a_{3x} = \sqrt{2}X_{cx}\Big/\left(V_{lx}/TR_x\right),$$
$$a_{4x} = 3N\left(V_{lx}\right)^2\Big/4\pi X_{cx}\left(TR_x\right)^2,\ a_{5x} = \pm H_{dcx0}^{-1}, \quad (A1)$$

$$b_{1x} = -a_{1x}\sin\beta_0,\ b_{2x} = -\sin\beta_0 + \sin\left(\beta_0 + \mu_{x0}\right), \quad (A2)$$
$$b_{3x} = \sin\left(\beta_0 + \mu_{x0}\right),\ b_{4x} = a_{5x}\left\{-2\sin\left(2\beta_0\right) + 2\sin 2\left(\beta_0 + \mu_{x0}\right)\right\},$$
$$b_{5x} = a_{5x}2\sin 2\left(\beta_0 + \mu_{x0}\right),$$

$$c_{1r} = \left(b_{1r}b_{3r}V_{dcr0} + a_{2r}b_{3r}b_{4r} - a_{2r}b_{2r}b_{5r} - a_{4r}a_{5r}b_{1r}\right), \quad (A3)$$
$$c_{2r} = \left(a_{2r}b_{3r}I_{dcr0} - b_{3r}V_{dcr0} + a_{4r}b_{5r}\right),$$

$$c_{1i} = V_{dci0} - a_{2i}I_{dci0},\ c_{2i} = b_{2i}b_{5i} - b_{3i}b_{4i} - b_{1i}b_{3i}I_{dci0}, \quad (A4)$$

where the letter set of (x, β, H) corresponds to (r, α, V) and (i, γ, I) for the rectifier and inverter, respectively. The coefficients for the state-space model (34) and (35) are represented as:

$$\mathbf{A} = \begin{bmatrix} & [\mathbf{A_1}] & [\mathbf{O}]_{1\times5} & [\mathbf{O}]_{2\times1} \\ & [\mathbf{O}]_{1\times5} & [\mathbf{A_1}] & 1 \\ [\mathbf{O}]_{14\times3} & [\mathbf{A_2}] & [\mathbf{O}]_{5\times5} & [\mathbf{A_4}] \\ & [\mathbf{O}]_{5\times4} & [\mathbf{A_3}] & [\mathbf{A_5}] \\ & [\mathbf{A_6}] & [\mathbf{O}]_{1\times5} & -1/T_k \end{bmatrix}, \quad (A5)$$

$$[\mathbf{A_1}]=\begin{bmatrix}1 & [\mathbf{O}]_{1\times4}\\ 0 & [\mathbf{O}]_{1\times4}\end{bmatrix},\quad [\mathbf{A_4}]=\begin{bmatrix}[\mathbf{O}]_{4\times1}\\ 1/k_iT_iV_{dci0}\end{bmatrix},\quad [\mathbf{A_5}]=\begin{bmatrix}[\mathbf{O}]_{4\times1}\\ -1/k_rT_rI_{dcr0}\end{bmatrix},$$

$$[\mathbf{A_2}]=\begin{bmatrix}-D_i/M_i & 0 & 1/M_i & 0 & 1/M_i\\ -1/R_{gi}T_{gi} & -1/T_{gi} & 0 & 0 & 0\\ 0 & 1/T_{ti} & -1/T_{ti} & 0 & 0\\ -V_iD_i/M_iT_{fi} & 0 & V_i/M_iT_{fi} & -1/T_{fi} & V_i/M_iT_{fi}\\ -1/R_iT_iV_{dci0} & 0 & 0 & -1/T_iV_{dci0} & -1/T_i\end{bmatrix},$$

$$[\mathbf{A_6}]=\begin{bmatrix}[\mathbf{O}]_{1\times4} & -2R/T_k\end{bmatrix},\quad [\mathbf{A_3}]=\begin{bmatrix}-1/M_r & -D_r/M_r & 0 & -1/M_r & 0 & 0\\ 0 & -1/R_{gr}T_{gr} & -1/T_{gr} & 0 & 0 & 0\\ 0 & 0 & 1/T_{tr} & -1/T_{tr} & 0 & 0\\ -V_r/M_rT_{fr} & -V_rD_r/M_rT_{fr} & 0 & V_r/M_rT_{fr} & -1/T_{fr} & 0\\ 0 & 1/R_rT_rI_{dcr0} & 0 & 0 & 1/T_rI_{dcr0} & -1/T_r\end{bmatrix},$$

$$\mathbf{B_E}=\mathbf{B_{1E}}+\mathbf{B_{2E}}=\begin{bmatrix}[\mathbf{O}]_{3\times6}^T & [\mathbf{B_1}]^T & [\mathbf{B_2}]^T & [\mathbf{O}]_{1\times6}^T\end{bmatrix}^T, \tag{A6}$$

$$[\mathbf{B_1}]=\begin{bmatrix}[\mathbf{O}]_{1\times4} & -1/M_i & 0\\ 1/T_{gi} & 0 & [\mathbf{O}]_{1\times4}\\ & [\mathbf{O}]_{1\times6} & \\ [\mathbf{O}]_{1\times4} & -V_i/M_iT_{fi} & 0\\ [\mathbf{O}]_{1\times2} & 1/T_iV_{dcr0} & [\mathbf{O}]_{1\times3}\end{bmatrix},\quad [\mathbf{B_2}]=\begin{bmatrix}[\mathbf{O}]_{1\times4} & 0 & -1/M_r\\ 0 & 1/T_{gr} & [\mathbf{O}]_{1\times4}\\ & [\mathbf{O}]_{1\times6} & \\ [\mathbf{O}]_{1\times4} & 0 & -V_r/M_rT_{fr}\\ [\mathbf{O}]_{1\times3} & 1/T_rI_{dcr0} & [\mathbf{O}]_{1\times3}\end{bmatrix},$$

$$\mathbf{C_E}=\begin{bmatrix}[\mathbf{O}]_{1\times3} & 1 & [\mathbf{O}]_{1\times10}\\ [\mathbf{O}]_{1\times8} & 1 & [\mathbf{O}]_{1\times5}\\ [\mathbf{O}]_{1\times13} & 1 & \\ [\mathbf{C_1}] & [\mathbf{O}]_{3\times10} & \end{bmatrix},\quad \text{and}\quad [\mathbf{C_1}]=\mathbf{I}_{3\times3},\quad \mathbf{D_E}=[\mathbf{O}]_{6\times4}. \tag{A7}$$

REFERENCES

[1] A. Ferrante *et al*., "The Mediterranean master plan consolidating a secure and sustainable electricity infrastructure in the Mediterranean region," in *Proc. 2018 CIGRE*, Paris, Aug. 2018, pp. 1–12.

[2] S. Favuzza *et al*., "New energy corridors in the Euro-Mediterranean area: the pivotal role of Sicily," *Energies*, vol. 11, no. 6, pp. 1–14, Jun. 2018.

[3] N. Anderson. (2016, Aug.). Shetland HVDC link project. Scottish and Southern Energy, Scotland. [Online]. Available: http://www.ssen-transmisson.co.uk/media/1514/shetland-hvdc-link-consultation-summary-booklet-august-2016.pdf

[4] D. Osborn. (2017, Apr.). MISO Transmission Planning Processes. Midcontinent Independent System Operator, Carmel, IN. [Online]. Available: https//www.cne.cl/wp-content/uploads/2017/04/Dale- Osborn.pdf

[5] R. Li *et al*., "Frequency control design for offshore wind farm grid with LCC-HVDC link connection," *IEEE Trans. Power Electron*., vol. 23, no. 3, pp. 1085–1092, May 2008.

[6] Z. Miao *et al*., "Wind farms with HVdc delivery in inertial response and primary frequency control," *IEEE Trans. Energy Convers*., vol. 25, no. 4, pp. 1171–1178, Dec. 2010.

[7] A. Yogarathinam *et al*., "Impact of inertia and effective short circuit ratio on control of frequency in weak grids interfacing LCC-HVDC and DFIG-based wind farms," *IEEE Trans. Power Del*., vol. 32, no. 4, pp. 2040–2051, Aug. 2017.

[8] L. Wang and M. Sa-Nguyen Thi, "Stability enhancement of a PMSG-based offshore wind farm fed to a multi-machine system through an LCC-HVDC link," *IEEE Trans. Power Syst.*, vol. 28, no. 3, pp. 3327–3334, Aug. 2013.

[9] Y. Wen *et al*., "Enhancing frequency stability of asynchronous grids interconnected with HVDC links," *IEEE Trans. Power Syst*., vol. 33, no. 2, pp. 1800–1810, Mar. 2018.

[10] S. G. Vennelaganti *et al*., "New insights into coupled frequency dynamics of AC grids in rectifier and inverter sides of LCC-HVDC interfacing DFIG-based wind farms," *IEEE Tran. Power Del.*, vol. 33, no. 4, pp. 1765–1776, Aug. 2018.

[11] S. P. Azad, R. Iravani, and J. E. Tate, "Damping inter-area oscillations based on a model predictive control (MPC) HVDC supplementary controller," *IEEE Trans. Power Syst.*, vol. 28, no. 3, pp. 3174–3183, Aug. 2013.

[12] S. P. Azad *et al*., "Decentralized supplementary control of multiple LCC-HVDC links," *IEEE Trans. Power Syst.*, vol. 31, no. 1, pp. 572–580, Jan. 2016.

[13] A. Gustafsson *et al*., "The new 525 kV extruded HVDC cable system," *ABB Grid Systems Technical Paper*, pp. 1–8, Aug. 2014.

[14] M. Saltzer *et al*., "Surge and extended overvoltages testing of HVDC cable systems," in *Proc. Int. Conf. Insulated Power Cables (Jicable' 17)*, Dunkerque, France, Nov. 2017, pp. 94–101.

[15] J. Zhu *et al*., "Inertia emulation control strategy for VSC-HVDC transmission systems," *IEEE Trans. Power Syst.*, vol. 28, no. 2, pp. 1277–1287, May. 2013.

[16] A. Junyent-Ferr, Y. Pipelzadeh, and T. C. Green, "Blending HVDC-link energy storage and offshore wind turbine inertia for fast frequency response," *IEEE Trans. Sustain. Energy*, vol. 6, no. 3, pp. 1059–1066, Jul. 2015.

[17] D. Kwon *et al*., "Modeling and analysis of an LCC HVDC system using DC voltage control to improve transient response and short-term power transfer capability," *IEEE Trans. Power Del.*, vol. 33, no. 4, pp. 1922–1933, Aug. 2018.

[18] Y. Xue *et al.*, "Reactive power and AC voltage control of LCC HVDC system with controllable capacitors," *IEEE Trans. Power Syst.*, vol. 32, no. 1, pp. 753–764, Jan. 2017.

[19] C Karawita *et al*., "Multi-infeed HVDC interaction studies using small-signal stability assessment," *IEEE Trans. Power Del.*, vol. 24, no. 2, pp. 910–918, Apr. 2009.

[20] D. Yoon *et al*., "Smart operation of HVDC systems for large penetration of wind energy resources," *IEEE Trans. Smart Grid*, vol. 4, no. 1, pp. 359–366, Mar. 2013.

[21] H. Atighechi *et al*., "Dynamic Average-Value Modeling of CIGRE HVDC Benchmark System," *IEEE Trans. Power Del*., vol. 29, no. 5, pp. 2046–2054, Oct. 2014.

[22] G. Morin *et al*., "Modeling of the hydro-Quebec - New England HVDC system and digital controls with EMTP," *IEEE Trans. Power Del.*, vol. 8, no. 2, pp. 559–566, Apr. 1993.

[23] F. Kong *et al*., "Development of a novel protection device for bipolar HVDC transmission lines," *IEEE Trans. Power Del.*, vol. 29, no. 5, pp. 2270–2278, Oct. 2014.

[24] H. T. Wang *et al*., "Stability mechanism analysis of HVDC control system for power system restoration using HVDC," in *Proc. 4th Int. Conf. Electric Utility Deregulation Restructuring Power Technol.*, Weihai, China, Jul. 2011, pp. 433–437.

[25] H. Liu and J. Sun, "Modeling and analysis of dc-link harmonic instability in LCC HVDC systems," in *Proc. IEEE 14th Workshop on Control and Modeling for Power Electronics (COMPEL)*, Salt Lake City, UT, Jun. 2013, pp. 1–9.

[26] M. Vasiladiotis and A. Rufer, "Dynamic analysis and state feedback voltage control of single-phase active rectifiers with dc-link resonant filters," *IEEE Trans. Power Electron*., vol. 29, no. 10, pp. 5620–5633, Oct. 2014.

[27] S. M. Muyeen *et al*., "Operation and control of HVDC-connected offshore wind farm," *IEEE Trans. Sustain. Energy*, vol. 1, no. 1, pp. 30–37, Apr. 2010.

[28] P. Kundur, *Power System Stability and Control*, Toronto, ON, Canada: McGraw-Hill, 1994, pp. 463–626.

[29] R. E. Kalman, "A new approach to linear filtering and prediction problems," *J.Basic Eng.*, vol. 82, no. 1, pp. 35–45, Mar. 1960.

[30] Y. Song and C. Breitholtz, "Nyquist stability analysis of an AC-grid connected VSC-HVDC system using a distributed parameter DC cable model," *IEEE Trans. Power Del*., vol. 31, no. 2, pp. 898–907, Apr. 2016.

[31] M. K. Bucher *et al*., "Fault current interruption in multiterminal HVDC networks," *IEEE Trans. Power Del.*, vol. 31, no. 1, pp. 87–95, Feb. 2016.

[32] T. K. Vrana *et al*., "The CIGRE B4 DC grid test system", *Electra*, vol. 270, pp. 10–19, Oct. 2013.

[33] F. Kong *et al*., "Development of a novel protection device for bipolar HVDC trans- mission lines," *IEEE Trans. Power Del.*, vol. 29, no. 5, pp. 2270–2278, Oct. 2014.

[34] G. Jang *et al*., "Novel reactive-power-compensation scheme for the Jeju-Haenam HVDC system," *IEE Proc.- Gener. Transm. Distrib.*, vol. 152, pp. 514–520, Jul. 2005.

[35] C. K. Kim *et al*., "Transient performance of Cheju-Haenam HVDC system," in *Proc. IEEE Power Eng. Soc. Summer Meeting*, Vancouver, BC, Jul. 2001, pp. 343–348.

[36] S. Hwang *et al*., "Evaluation of STATCOM capacity on transient stability in Jeju-island system with HVDC and wind farms," in *Proc. 9th International Conf. Power Electronics and ECCE Asia (ICPE-ECCE Asia)*, Seoul, Jul. 2015, pp. 367–372.

[37] D. Kwon *et al*., "Modeling of HVDC System to improve estimation of transient DC current and voltages for AC line-to-ground fault – an actual case study in Korea," *Energies*, vol. 10, no. 10, pp. 1–18, Oct. 2017.

[38] Fast Response Regulation Signal, PJM [Online]. Available: http://www.pjm.com/markets-and-operations/ancillary-services/mkt-based-regulation/fast-response-regulation-signal.aspx

[39] D. S. Carvalho *et al*., "Final project planning conception for the first 800 kV HVDC link of Belo Monte," in *Proc. 2014 CIGRE*, Paris, Aug. 2014, pp. 1–9.

[40] P. Morshuis *et al*., "Stress conditions in HVDC equipment and routes to in service failure," *IEEE Trans. Dielectr. Electr. Insul.*, vol. 22, no. 1, pp. 81–91, Feb. 2015.

[41] P. Maussion *et al*., "Lifespan and aging modeling methods for insulation systems in electrical machines: A survey," in *Proc. IEEE Workshop Elect. Mach. Des. Control Diagnosis*, Torino, Mar. 2015, pp. 279–288.

[42] V. I. J. Kokko, "Ageing due to thermal cycling by start and stop cycles in lifetime estimation of hydroelectric generator stator windings," in *Proc. IEEE International Electric Machines & Drives Conference (IEMDC)*, Marseille, May 2011, pp. 318–323.

Do-Hoon Kwon (S'15) received the B.S., M.S., and Ph.D. degrees in electrical engineering from Seoul National University, Seoul, South Korea, in 2010, 2012, and 2018, respectively. He is currently a Senior Researcher in the Smart Power Grid Research Center, Korea Electrotechnology Research Institute (KERI), Uiwang, South Korea. His research interests include HVdc systems, energy management systems, and smart distribution systems.

Dr. Kwon was selected as a recipient of the Best Reviewer for the IEEE TRANSACTIONS ON SMART GRID in 2017.

Young Jin Kim (S'14–M'15) **Young-Jin Kim** (Member, IEEE) received the B.S. and M.S. degrees in electrical engineering from Seoul National University in 2007 and 2010, respectively, and the Ph.D. degree in electrical engineering from the Massachusetts Institute of Technology in 2015. He worked with Korea Electric Power Corporation as a Power Transmission and Distribution System Engineer from 2007 to 2011. He was also a Visiting Scholar with the Catalonia Institute for Energy Research in 2014, and a Postdoctoral Researcher with Center for Energy, Environmental, and Economic Systems Analysis, Energy Systems Division, Argonne National Laboratory from 2015 to 2016. He joined the faculty of the Pohang University of Science and Technology, where he is currently an Associate Professor with the Department of Electrical Engineering. His research fields of interest include distributed generators, renewable energy resources, and smart buildings.

Dr. Kim is a recipient of the Best Reviewer for the IEEE TRANSACTIONS ON SMART GRID in 2019. He is an Editor of the IEEE TRANSACTIONS ON SMART GRID.

Oriol Gomis-Bellmunt (S'05-M'07-SM'12) received the degree in industrial engineering from the School of Industrial Engineering of Barcelona (ETSEIB), Technical University of Catalonia (UPC), Barcelona, Spain, in 2001 and the Ph.D. degree in electrical engineering from the UPC in 2007. In 1999, he joined Engitrol S.L. where he worked as Project Engineer in the automation and control industry. Since 2004, he has been with the Electrical Engineering Department, UPC where he is a Professor and participates in the CITCEA-UPC Research Group. Since 2020, he is an ICREA Academia researcher. His research interests include the fields linked with electrical machines, power electronics, and renewable energy integration in power systems.